Surface and average volume temperature measurements in semitransparent media based on multispectral thermotransmittance

C. Bourgès [a,b], J. Maire [a,b,*], S. Chevalier [a,b,*], S. Dilhaire [c]

[a] Univ. Bordeaux, CNRS, Bordeaux INP, I2M UMR 5295, Talence, 33400, France
[b] ENSAM, CNRS, Bordeaux INP, I2M, UMR 5295, Talence, 33400, France
[c] Univ. Bordeaux, CNRS, LOMA UMR 5798, Talence, 33400, France

Keywords:
Heat transfer
Infrared transmission imaging
Thermography
Semitransparent media
Thermomodulation
Material properties
Temperature measurements

A B S T R A C T

Temperature plays an essential role in maintaining the performance of microsystems, which calls for three-dimensional mapping of heat sources, hot spots and thermal properties. In this context, infrared (IR) thermography provides information for opaque materials but faces limitations when applied to semitransparent samples such as microfluidic chips or semiconductor materials in the IR range. In this article, we present temperature maps obtained for the surface and average volume of two semitransparent samples with a detection limit of 1 K. To achieve such measurements, we demonstrated that thermotransmittance signals can be decomposed into two parts: the first originating from interfaces and the second originating from the volume. We quantified the contributions of both components by combining contactless measurements with a heat transfer model. We then validated the method using two Borofloat glass samples with different thicknesses. We were able to discriminate the contributions of surface and volume temperatures by performing spectroscopic thermotransmittance measurements at wavelengths ranging from 3100 to 3400 nm due to the different spectral behaviors of these two components. This new technique is an important improvement for temperature measurements using IR cameras in semitransparent media.

1. Introduction

Temperature plays an essential role in maintaining the performance of microsystems, including batteries, microfluidic cells, and supercapacitors, as it influences energy storage, generation, conversion, and dissipation within these systems [1]. Therefore, contactless temperature measurements during system operation are essential for monitoring and enhancing such devices. The most developed techniques rely on surface measurements of opaque media, such as infrared thermography [2–5], which detects infrared radiation emitted by a sample at a given temperature. Another approach is thermoreflectance [6,7], which measures the variations in light intensity reflected from the sample's surface relative to temperature changes. Such surface measurements, provided they are calibrated, can be combined with thermal models and inverse methods [8,9] to obtain the temperature at the depth of the device, given its known geometry. However, the probed depth is constrained by measurement noise when employing inverse methods [10]. In addition, IR thermography is not well adapted to semitransparent media because infrared radiation originates from both the surface and the volume of the sample [11]. Moreover, background radiation must be filtered out [12]. Consequently, the growing use of infrared semitransparent materials in microsystems, such as semiconductors or glass substrates, requires specific methods for contactless temperature measurements.

In semitransparent materials, common techniques measure the average temperature within the volume of the sample along the path of a probing wave. For instance, magnetic resonance imaging (MRI) [13,14] and ultrasonic thermometry [15] focus on transparent media in radio-frequency and ultrasound spectral ranges, respectively. By scanning the sample under different viewing angles or combining several imaging techniques [16,17], the 3D temperature field can be reconstructed using dedicated algorithms. However, MRI is an expensive technique and is not suitable for all media. However, ultrasonic thermometry is a point-by-point technique, and quantitative results highly depend on calibration and materials [18]: there is no universal method for temperature probing within a device, especially for semitransparent media. Nevertheless, whereas the advantage of semitransparent materials is that transmitted light can be detected, the origin of the signal or its variations are challenging to determine.

In our previous works [19,20], we investigated the use of thermotransmittance to measure temperature in infrared semitransparent media. Other works have shown that this technique can be used in

* Corresponding authors.
E-mail addresses: jeremie.maire@u-bordeaux.fr (J. Maire), stephane.chevalier@u-bordeaux.fr (S. Chevalier).

https://doi.org/10.1016/j.ijheatmasstransfer.2024.126087

various spectral ranges, including the visible [21], near-infrared [22] or terahertz [23] regions, demonstrating its potential application across a wide range of materials and applications. The principle consists of illuminating a sample with an incident light beam and measuring the signal transmitted through the sample. The transmitted flux depends on the optical properties of the material, such as the reflectance at the interfaces and the absorbance within the volume. The optical properties are temperature dependent, as is the case for the transmitted signal. The first-order thermotransmittance signal can be approximated as linear with respect to temperature. When the temperature is uniform along the optical path within the sample, the thermotransmittance coefficient, $\kappa(\lambda)$, is a wavelength-dependent proportionality factor between the variations in temperature and transmission. This coefficient does not indicate what happens at the interfaces or within the volume of the sample.

In the general case, however, thermal gradients exist within the sample volume, and the thermotransmittance coefficient provides an oversimplified view of the temperature. Consequently, the thermotransmittance signal must be decomposed into two parts: one coming from the interfaces due to the reflectance and the other from the volume with the absorbance of the material. The Appendix A gives more details about the origin of the thermotransmittance signal [24]. The thermotransmittance coefficient is then replaced by two thermo-optic coefficients: $\kappa_R(\lambda)$ (K^{-1}), which refers to the temperature variations of the interfaces, and $\kappa_A(\lambda)$ (K^{-1}), which refers to the average volume temperature. In this article, we demonstrate that the thickness L_z influences the value of the coefficient $\kappa_A(\lambda)$. Consequently, we introduce an intrinsic coefficient $\kappa_{A,i}(\lambda)$ ($K^{-1}m^{-1}$) normalized by the material thickness. Finally, if $\kappa_{A,i}(\lambda)$ and $\kappa_R(\lambda)$ are uncorrelated within the studied spectral range, spectroscopic thermotransmittance enables the simultaneous measurement of interfaces and average volume temperature.

The main challenge regarding thermotransmittance is the weakness of the measured signal, $\kappa \approx 10^{-4}$ K^{-1}, which leads to an extreme sensitivity to electronic noise, parasitic signals, and drifts. This sensitivity results in (i) the use of modulated signals to remove parasitic noise and improve the signal-to-noise ratio (SNR) and (ii) the need for a calibration step to perform temperature measurements to overcome the lack of a database regarding thermo-optic coefficients κ_R and κ_A.

The aim of this work is to measure the coefficients κ_R and κ_A using a calibration procedure and then demonstrate that multispectral thermotransmittance allows simultaneous determination of the surface and average volume temperature of a semitransparent medium. In this article, we first introduce the experimental setup used to perform thermotransmittance measurements at the microscopic scale and the thermal model used for thermo-optic coefficient calibration. To validate the method, measurements are conducted on two Borofloat glass wafers with different thicknesses L_z. While the surface coefficient κ_R must remain constant for both samples, the volume coefficient κ_A will vary. However, the intrinsic coefficient, $\kappa_{A,i}$ ($K^{-1}m^{-1}$), normalized by the thickness, will remain independent of the thickness. Following the validation procedure, we present the measured temperature maps of the top surface and the average volume for the two samples.

2. Method

The thermotransmittance signal is measured by illuminating a sample and detecting the changes in light transmission induced by temperature variations along its optical path. In the authors' previous work [19], we investigated the case of a homogeneous temperature along the optical path and demonstrated that the relative variation in the transmittance, $\Delta\Gamma/\Gamma_0$, is related to the variation in the average sample temperature ΔT:

$$\frac{\Delta\Gamma}{\Gamma_0}(\lambda) = \kappa(\lambda)\Delta T, \tag{1}$$

where κ is the thermotransmittance coefficient (K^{-1}) and Γ_0 is the transmittance at T_0. The expression is valid for samples with homogeneous temperature along the optical path. In a more general case, the thermotransmittance expression must be split into two parts (see Appendix A):

$$\frac{\Delta\Gamma}{\Gamma_0}(\lambda) = \kappa_R(\lambda)\Delta T^S + \kappa_A(\lambda)\Delta T^V, \tag{2}$$

where ΔT^S (K) is the temperature variation at the interfaces of the sample and ΔT^V (K) is the average temperature variation within the sample volume. In this section, we present the thermotransmittance setup and the thermal model used to calibrate the thermo-optic coefficients κ_R and κ_A.

2.1. Experimental setup

The modulated thermotransmittance setup consists of illuminating the sample with an incident flux, modulating the temperature of the sample, and detecting the variations in the flux transmitted through the sample at the frequency of the temperature modulation [19]. Fig. 1 illustrates the procedure. First, the sample is illuminated with an IR flux, ϕ_0 (W/m^2), from a black body (IR-Si217) heated at 1385 °C. The radiation is filtered out in a diffraction grating monochromator (Bentham Instruments TMc300), which enables us to select the wavelength of illumination, λ (m). To work with an acceptable signal-to-noise ratio (SNR), a compromise must be established between the spectral sensitivity of the acquisition chain and the transmittance function $\Gamma(\lambda)$ of the sample, as illustrated in Fig. 2. Consequently, we work in the spectral range $\lambda \in [3100\text{–}3400]$ nm.

To detect the flux transmitted through the sample over time, $\phi_0\Gamma(\lambda,t)$, we use an IR camera (FLIR SC7000) with an indium-antimonide sensor with 512 × 640 pixels and a pitch of 15 µm. The camera is equipped with a microscope objective, resulting in an image spatial resolution of 15 µm/pixel. However, the camera measures the transmitted flux of interest, $\phi_0\Gamma(\lambda,t)$, as well as the infrared radiation coming from both the environment and the sample itself, depending on its temperature. To remove this latter signal, the camera is synchronized with a mechanical chopper, which modulates the light at a frequency of 150 Hz. The signal demodulation at the chopper frequency filters out the parasitic radiation from the measured signal.

As mentioned in the introduction, the studied samples are two Borofloat wafers with thicknesses of $L_z = 2$ mm and 3.3 mm, and their spectral transmittance is given in Fig. 2. To heat these samples at the micrometer scale, thin gold resistors with a thickness of 300 nm and width of $e = 30$ µm are deposited on the top surface of the wafers. A sinusoidal current, $I(t) = I_\omega\cos(\omega t)$, is injected into the resistor using a Keithley 6221 current source, and the sample is heated by the Joule effect. The temperature is thus modulated at twice the current frequency, 2ω:

$$T(x,y,z,t) = T_0(x,y,z,t) + T_{2\omega}(x,y,z)\cos(2\omega t + \phi(x,y,z)) \tag{3}$$

The thermotransmittance is proportional to the temperature variations; therefore, the transmittance $\Gamma(x,y,\lambda,t)$ is modulated at frequency 2ω. The fast Fourier transform (FFT) algorithm decomposes the measured signal by frequency. Analysis of the frequency spectrum gives the amplitude $\Gamma_{2\omega}$ and mean signal Γ_0 (see the right graph in Fig. 1 insert). Then, the ratio $\Gamma_{2\omega}/\Gamma_0$ at several wavelengths allows us to retrieve both the surface and volume temperatures of the sample, provided that we know the coefficients κ_R and κ_A. Consequently, the first step is measuring these coefficients with a calibration procedure.

Extracting the thermo-optic coefficients from the thermotransmittance signal requires a known reference temperature. We measure the voltage at the resistor terminals and use the 3ω method [25,26] to obtain the resistor temperature variation at frequencies 2ω and $T_{R2\omega}$. The expression of $T_{R2\omega}$ is given in Eq. (4), where $U_{3\omega}$ (V) is the voltage component at frequency 3ω, R_0 is the electrical resistance of the gold

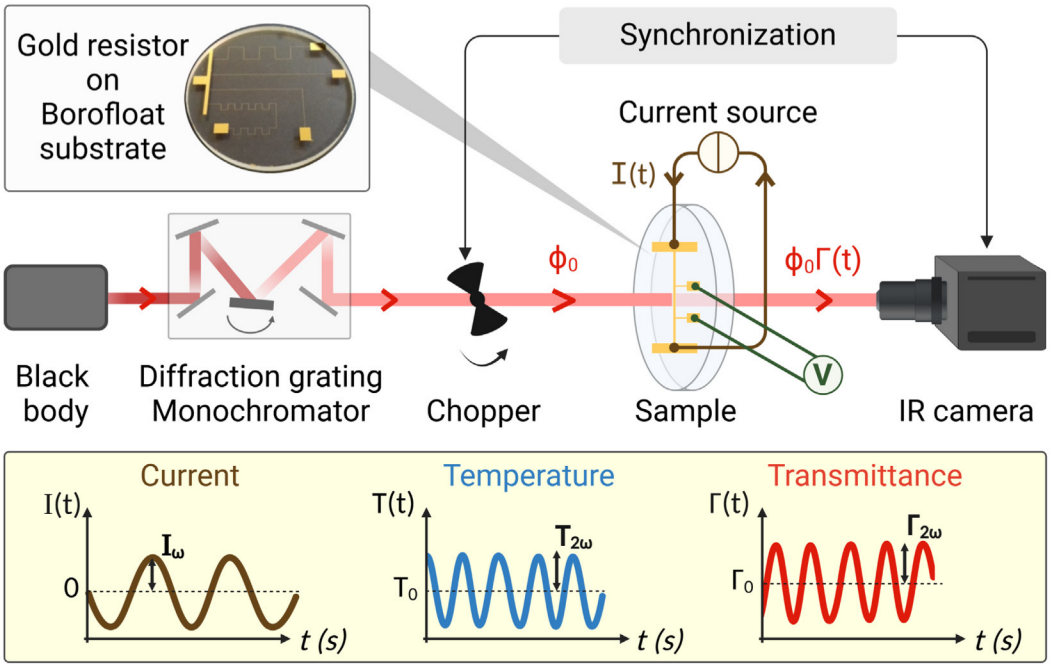

Fig. 1. Experimental setup for microscopic modulated thermotransmittance imaging. The yellow insert presents the different measured signals and the nomenclature used. The insert on the left shows the Borofloat sample with the thin gold resistors at its top surface. (For interpretation of the references to color in this figure legend, the reader is referred to the web version of this article.)

deposit (Ω), I_ω (A) is the amplitude of the current injected into the resistor, and $\beta = 3.10^{-3}$ (K^{-1}) is the previously calibrated temperature coefficient for the resistance of gold.

$$T_{R2\omega} = 2\frac{U_{3\omega}}{R_0 I_\omega \beta} \tag{4}$$

2.2. Heat transfer model

For calibrating the coefficients κ_R and κ_A, we require the temperature distribution within the sample and compare it with the thermotransmittance measurements. In Fig. 3(a), we present the simplified 3D geometry of the sample with the boundary conditions used in the thermal modeling. Assuming symmetry in the temperature distribution on both sides of the gold resistor and constant temperature along the y-axis far from the resistor's terminals, we simplify the problem to a 2D model along the x and z axes, as shown in Fig. 3(b). In addition, convective losses are negligible, as explained in Appendix B.

The transient heat transfer equation in the (x, z) coordinates and its associated boundary conditions are detailed in the system from Eqs. (5) to (9). Here, a is the thermal diffusivity (m^2/s), k is the thermal conductivity (W/m/K), $\varphi(x,t)$ is the thermal flux delivered by the gold resistor (W/m^2), and T_{amb} is the ambient temperature (K).

$$\begin{cases} \dfrac{\partial^2 T(x,z,t)}{\partial x^2} + \dfrac{\partial^2 T(x,z,t)}{\partial z^2} = \dfrac{1}{a}\dfrac{\partial T(x,z,t)}{\partial t} & (5) \\ -k\dfrac{\partial T(x,z,t)}{\partial z}\Big|_{z=0} = \varphi(x,t) & (6) \\ \dfrac{\partial T(x,z,t)}{\partial z}\Big|_{z=L_z} = 0 & (7) \\ \dfrac{\partial T(x,z,t)}{\partial x}\Big|_{x=0} = \dfrac{\partial T(x,z,t)}{\partial x}\Big|_{x=L_x} = 0 & (8) \\ T(x,z,t=0) = T_{amb} & (9) \end{cases}$$

Because we are interested only in the temperature variation at frequency 2ω, the initial step involves decomposing the incoming flux, $\varphi(x,t)$, and the temperature field by frequency (see Eqs. (3) and (10)).

$$\varphi(x,t) = \varphi_0 H(x)\cos(2\omega t) \tag{10}$$

H is a Heaviside distribution function: $H(x) = 1$ for $x \in [0; e/2]$ and 0 elsewhere, where e is the width of the resistor. Consequently, at frequency 2ω, the heat transfer problem is formulated by a system of equations from (11) to (14).

$$\begin{cases} \dfrac{\partial^2 T_{2\omega}(x,z)}{\partial x^2} + \dfrac{\partial^2 T_{2\omega}(x,z)}{\partial z^2} = \dfrac{i2\omega}{a} T_{2\omega}(x,z) & (11) \\ -k\dfrac{\partial T_{2\omega}(x,z)}{\partial z}\Big|_{z=0} = \varphi_0 H(x) & (12) \\ \dfrac{\partial T_{2\omega}(x,z)}{\partial z}\Big|_{z=L_z} = 0 & (13) \\ \dfrac{\partial T_{2\omega}(x,z)}{\partial x}\Big|_{x=0} = \dfrac{\partial T_{2\omega}(x,z)}{\partial x}\Big|_{x=L_x} = 0 & (14) \end{cases}$$

Then, a cosine integral transform is applied to the spatial component x, as described by Eqs. (15) and (16), for the temperature variation and the incoming flux, respectively. The eigenvalues of the integral cosine transform are denoted as $\alpha_n = n\pi/L_x$, where $n = 0, 1, 2, \ldots$ [27].

$$\tilde{T}_{2\omega}(\alpha_n, z) = \int_0^{L_x} T_{2\omega}(x,z)\cos(\alpha_n x)\,dx \tag{15}$$

$$\tilde{\varphi}(\alpha_n) = \varphi_0 \int_0^{L_x} H(x)\cos(\alpha_n x)\,dx = \varphi_0 \frac{\sin(\alpha_n e/2)}{\alpha_n} \tag{16}$$

The final system is provided in Eqs. (17) to (19):

$$\begin{cases} \dfrac{d^2\tilde{T}_{2\omega}(\alpha_n,z)}{dz^2} - Q^2\tilde{T}_{2\omega}(\alpha_n,z) = 0 & (17) \\ -k\dfrac{d\tilde{T}_{2\omega}(\alpha_n,z)}{dz}\Big|_{z=0} = \tilde{\varphi}(\alpha_n) & (18) \\ \dfrac{d\tilde{T}_{2\omega}(\alpha_n,z)}{dz}\Big|_{z=L_z} = 0 & (19) \end{cases}$$

with $Q^2 = \alpha_n^2 + i2\omega/a$. The solution of this system is expressed as $\tilde{T}_{2\omega}(\alpha_n, z) = Ae^{Qz} + Be^{-Qz}$, where

$$A = -\tilde{\varphi}(\alpha_n)\frac{1}{kQ\left(1 - e^{2QL_z}\right)} \tag{20}$$

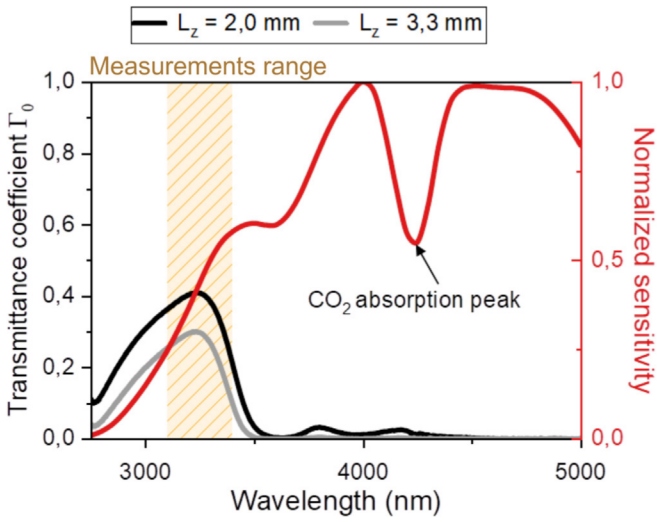

Fig. 2. Transmittance of the Borofloat wafer for two different thicknesses Ł$_z$ and spectral sensitivity of the acquisition chain (red). The measurement range is presented in orange. (For interpretation of the references to color in this figure legend, the reader is referred to the web version of this article.)

$$B = Ae^{2QL_z} \tag{21}$$

Finally, the temperature variation at 2ω in the spatial coordinate system (x, z) is obtained through the inverse cosine transform:

$$T_{2\omega}(x,z) = \frac{1}{L_x}\tilde{T}_{2\omega}(\alpha_0, z) + \frac{2}{L_x}\sum_{n=1}^{N}\tilde{T}_{2\omega}(\alpha_n, z)\cos(\alpha_n x) \tag{22}$$

The temperature variation at the top surface of the sample, $T^S_{2\omega}(x)$, and the average temperature variation within the volume, $T^V_{2\omega}(x)$, are given by:

$$T^S_{2\omega}(x) = T_{2\omega}(x, z=0) \tag{23}$$

$$T^V_{2\omega}(x) = \frac{1}{L_z}\int_0^{L_z} T_{2\omega}(x,z)dz \tag{24}$$

3. Results and discussion

3.1. Measured temperature field

To estimate the surface and volume temperatures, $T^S_{2\omega}$ and $T^V_{2\omega}$ (see Eqs. (23) and (24)), the temperature field is normalized by the expression $T_{2\omega}(x=0, z=0)$. Consequently, only the thermal diffusivity, a, thickness, L_z, and reference temperature are needed. The thermal diffusivity is determined using the phase of the thermotransmittance signal, as described in [24]. The result is $a = (7.5 \pm 0.5) \times 10^{-7}$ m^2/s, which is in good agreement with the supplier datasheet [28]. With respect to the temperature reference measured with the 3ω method, we assume that $T_{R2\omega} = T_{2\omega}(x=0, z=0)$. In this study, f_T is set to 80 mHz, and the temperature variations of the resistor are 18.5 ± 1.0 K and 22.0 ± 1.0 K for measurements conducted with samples with thicknesses of 2.0 mm and 3.3 mm, respectively.

Figs. 4(b) and (c) present the calculated temperature fields $T^S_{2\omega}(x, L_z = 3.3\,\text{mm})$ and $T^V_{2\omega}(x, L_z = 3.3\,\text{mm})$ across the range $x \in [0{-}2]$ mm, corresponding to the measurement area. The surface temperature variation decreases from 22 K at the hottest point to 2K 2 mm away from the hottest point. Consequently, the average volume temperature remains low compared to the surface temperature, ranging from slightly below 3 K to below 1 K (see Fig. 4(c)). Despite these low values, the next section demonstrates that we managed to measure the thermo-optic coefficients of the sample.

3.2. Thermo-optic coefficient extraction and impact of wavelength

To separate the contributions of surface (κ_R) and volume (κ_A), equation (2) is rewritten, resulting in Eq. (25): the temperature variations $T^S_{2\omega}$ and $T^V_{2\omega}$ are modeled (see Fig. 4), and the thermotransmittance signal $\Gamma_{2\omega}/\Gamma_0$ is measured using the experimental setup. Fig. 5(a) shows a map of the sample with a thickness of 3.3 mm.

$$\frac{\Gamma_{2\omega}(\lambda)}{\Gamma_0(\lambda)T^V_{2\omega}} = \kappa_R(\lambda)\frac{T^S_{2\omega}}{T^V_{2\omega}} + \kappa_A(\lambda) \tag{25}$$

Plotting the left term, $\Gamma_{2\omega}/\Gamma_0 T^V_{2\omega}$, as a function of the temperature ratio shows that the slope corresponds to the coefficient κ_R, while the y-intercept is the coefficient κ_A.

To improve the signal-to-noise ratio (SNR), the signal is averaged along the y-axis, as shown in Fig. 5(b), and from both sides of the resistor for symmetry considerations. Near the resistor, the signal is unusable due to the resolution limitation and camera vibrations. The data used for calibration started at a distance of 90 μm from the resistor. The calculated temperatures $T^S_{2\omega}$ and $T^V_{2\omega}$ are attributed to each pixel of the camera based on distance x from the gold resistor. Then, the thermotransmittance signal of each pixel is normalized by the corresponding value $T^V_{2\omega}(x)$ and plotted as a function of the ratio $T^S_{2\omega}/T^V_{2\omega}(x)$, resulting in Fig. 5(c). Finally, a linear regression is applied to extract the coefficients κ_R and κ_A. The residuals of the fit give satisfactory values, on average lower than 3% (see Fig. 5(d)). As expected, the further from the resistor (corresponding to smaller $T^S_{2\omega}/T^V_{2\omega}$ ratios), the higher the residuals due to a lower SNR.

The spectral measurements of κ_R and κ_A for samples with thicknesses of 2 mm and 3.3 mm are presented in Figs. 6(a) and (b). The first interesting point is the consistency of κ_R for the two samples, with an average value of $\kappa_R = (2.9 \pm 0.5) \times 10^{-4}$ K^{-1} highlighted by a green line in Fig. 6(a). Furthermore, κ_A increases with the wavelength for both samples. To link these trends to the optical properties of Borofloat, Fig. 6(c) illustrates the reflectance and absorbance spectra of the material at ambient temperature. When the reflectance remains constant, the absorbance varies by approximately a factor of 4 within the range of $\lambda \in [3100{-}3400]$ nm. Thus, the optical properties and the thermo-optic coefficients are correlated. Consequently, analyzing the optical properties of a material at ambient temperature provides a rough estimate of the behavior of its thermo-optic coefficients, which is crucial for selecting an appropriate working spectral range.

Although κ_A exhibits the same behavior with respect to the thickness L_z, an offset exists between the two datasets. However, this outcome was expected since the sample thickness influences the overall absorbance of the material. Therefore, we introduce the intrinsic coefficient $\kappa_{Ai} = \kappa_A/L_z$ (K^{-1}m^{-1}), which is normalized by the sample thickness (see Fig. 6(d)). Finally, κ_{Ai} is the same for the two samples of different thicknesses, which was expected since the same material was obtained from the same provider. As a result, the measurements of the thermo-optic coefficients relative to the reflectance, κ_R, and to the absorbance, κ_{Ai}, of the material remain valid regardless of thickness. For thin materials at the micrometric or nanometric scale, additional phenomena such as multiple light reflections within the sample may occur. Specific study should be performed for such samples.

3.3. Surface and average volume temperature maps in semitransparent media

Finally, since the spectral coefficients κ_R and κ_A are uncorrelated, we use multispectral thermotransmittance measurements to simultaneously assess both the surface and average volume temperature of the sample. The thermotransmittance signal of the samples is measured at several wavelengths [3100 – 3400] nm. The matrix system described in Eq. (26) gives the relation between the thermotransmittance signal, the calibrated thermo-optic coefficients, and the temperatures we aim to

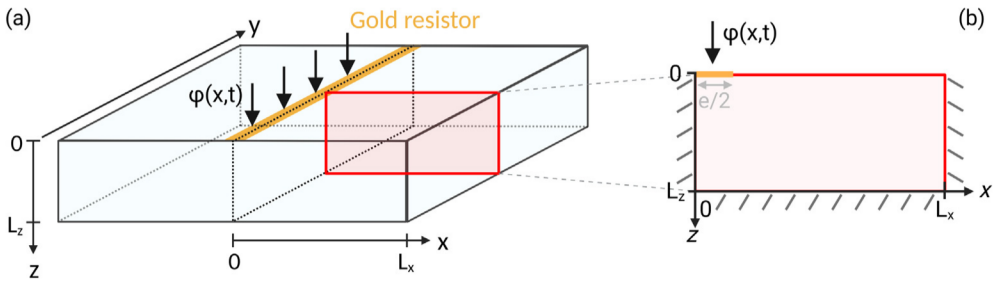

Fig. 3. (a) 3D geometry of the sample centered on the gold resistor and (b) simplified 2D geometry used in the model assuming symmetry on the two sides of the gold resistor and that the temperature is constant along the y-axis far from the resistor's terminals. (For interpretation of the references to color in this figure legend, the reader is referred to the web version of this article.)

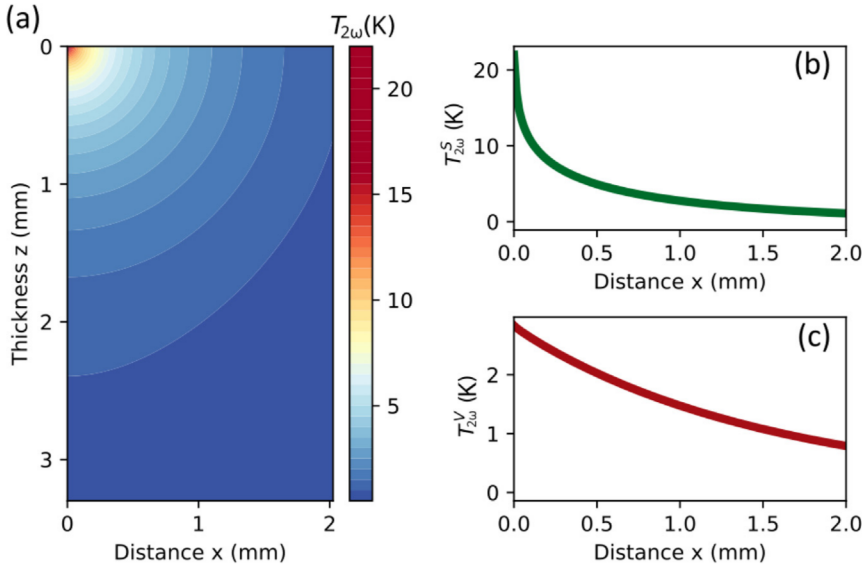

Fig. 4. Thermal modeling based on the measured values of a and $T_{2\omega}(x=0,z=0)$ of (a) the 2D temperature variation field $T_{2\omega}(x,z)$, (b) the top surface temperature profile $T^S_{2\omega}(x)$, and (c) the average volume temperature $T^V_{2\omega}(x)$ for a thickness of $L_z = 3.3$ mm.

measure for a single pixel with coordinates (x, y). Using a least-square algorithm [29] on the system (26), $X = [A^T A]^{-1} A^T Y$, we derive the temperature maps for both the top surface and average volume, as illustrated in Fig. 7.

$$\overbrace{\begin{bmatrix} \frac{\Gamma_{2\omega}}{\Gamma_0}(x,y,\lambda_1) \\ \dots \\ \frac{\Gamma_{2\omega}}{\Gamma_0}(x,y,\lambda_n) \end{bmatrix}}^{Y} = \overbrace{\begin{bmatrix} \kappa_R(\lambda_1) & \kappa_A(\lambda_1) \\ \dots & \dots \\ \kappa_R(\lambda_n) & \kappa_A(\lambda_n) \end{bmatrix}}^{A} \overbrace{\begin{bmatrix} T^S_{2\omega}(x,y) \\ T^V_{2\omega}(x,y) \end{bmatrix}}^{X} \tag{26}$$

The matrix S gives the uncertainty associated with the calculated temperatures, where σ_S is the uncertainty in the surface temperature, σ_V is the uncertainty in the volume temperature, and σ is the measurement error in the thermo-optic coefficients.

$$S = \begin{bmatrix} \sigma_S & \sigma_V \end{bmatrix} = \text{diag}\left(\sqrt{\sigma^2 [A^T A]^{-1}}\right) \tag{27}$$

As expected, the surface temperature variation is higher than the average volume temperature, at 15 K versus 2 K near the resistor. The surface temperatures shown in Figs. 7(a) and (b) are symmetrical on either side of the resistor and decrease rapidly with distance, as predicted by the model in Fig. 4(a). Regarding the average volume temperature of sample $L_z = 3.3$ (Fig. 7(c)), the variations are homogeneous: the model predicted a temperature variation of 1 K from $x = 0.3$ mm to $x = 2$ mm, which aligns with the measurement noise level of $\pm$ 1 K derived from the matrix S detailed in (27). By comparison, the average volume temperature of the 2.0 mm sample is also highly influenced by noise, but we observe a tendency: the average variations are greater close to the resistor and decrease with distance (see Fig. 7(d)). Despite the surface temperature of this sample being lower than that of the 3.3 mm sample, its thickness is 40% less, resulting in a higher average volume temperature.

In our case, due to small temperature variations with respect to the sensitivity, noise plays a crucial role in the measured signal. Moreover, thermotransmittance measurements are strongly impacted by the sample thickness. On the one hand, a greater thickness enhances the contribution of the absorbance to the signal, hence increasing the sensitivity to the average volume temperature. On the other hand, thicker samples result in low transmittance and consequently lower signal-to-noise ratio (SNR). In future works, more powerful heat sources, such as lasers, will be used to investigate thick and absorbent media.

4. Conclusion

In conclusion, this study demonstrates that multispectral thermotransmittance allows the simultaneous determination of surface and average volume temperatures within a semitransparent medium. To achieve this, we calibrate the thermo-optic coefficients κ_R and κ_A. Our methodology combines measurements at the micrometric scale, including the heating device, and a thermal model. The detection sensitivity of the current setup is 1 K with the Borofloat sample, nevertheless, with a material whose thermo-optic coefficients are lower, the minimum

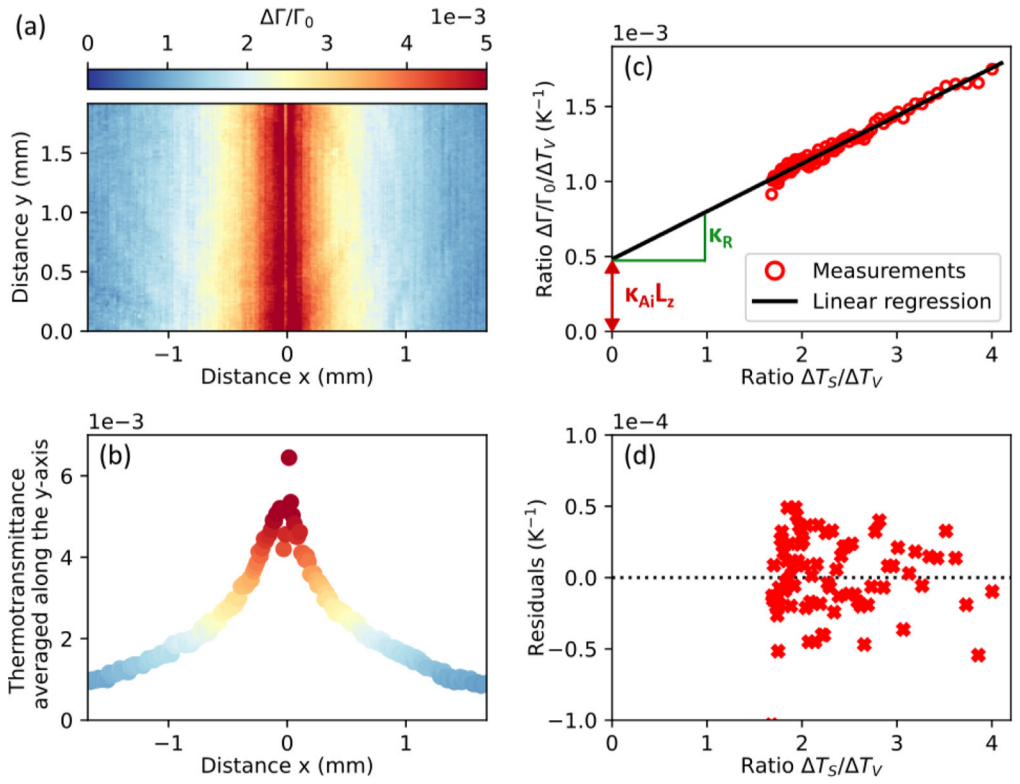

Fig. 5. (a) Measured 2D thermotransmittance along the x- and y-axes and the corresponding profile averaged along the *y*-axis (b) for the sample with a thickness of 3.3 mm at a wavelength of $\lambda = 3300$ nm. (c) $\Gamma_{2\omega}/\Gamma_0 T_{2\omega}^V$ versus temperature ratio: the slope is the coefficient κ_R, and the y-intercept is the coefficient κ_A. The residuals between the measurements and fit are plotted in graph (d), and the mean value is 0.07%.

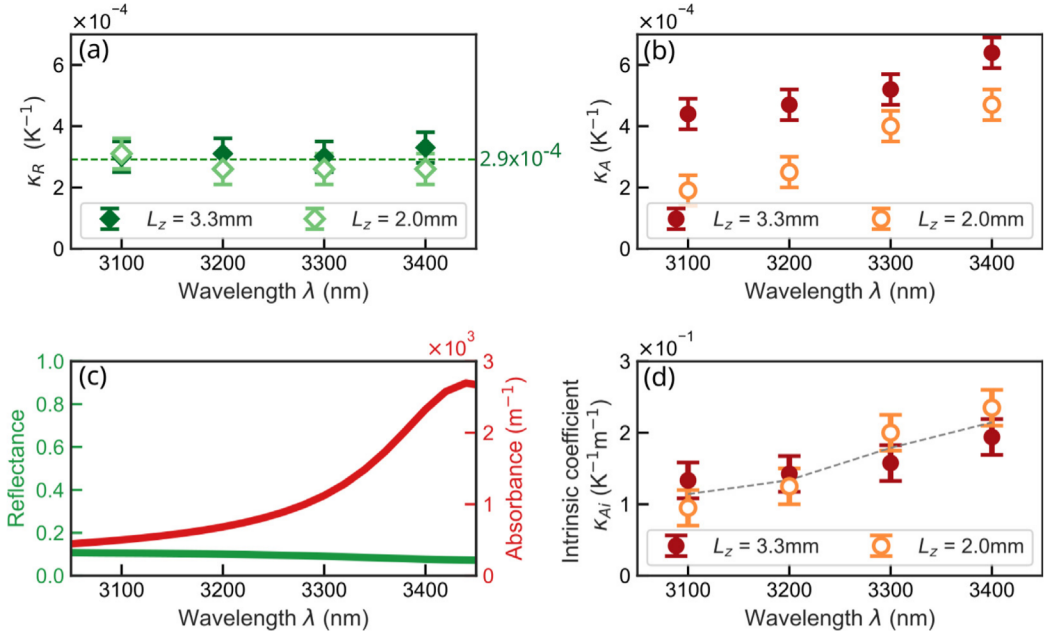

Fig. 6. Thermo-optic coefficients κ_R (a) and κ_A (b) (K^{-1}) measured for the samples with thicknesses of 2.0 mm and 3.3 mm. The green dotted line on graph (a) corresponds to the mean value of κ_R. (c) Reflectance and absorbance coefficient versus wavelength of the Borofloat glass measured for a sample with a thickness of 2.0 mm. (d) Intrinsic coefficient $\kappa_{Ai} = \kappa_A/L_z$ ($K^{-1}m^{-1}$) extracted from measurements of κ_A at thicknesses of 2.0 mm and 3.3 mm. The gray line corresponds to the mean value to help with the data analysis.

detectable variations would be higher and vice versa. To overcome this threshold, the use of powerful heat sources and probing lights is crucial for amplifying the thermotransmittance signal and enhancing the signal-to-noise ratio (SNR).

Our previous works focused on scenarios where the temperature distribution within the sample was homogeneous. Thus, the calibrated thermotransmittance coefficient disregards variations at interfaces and within the sample volume. Knowledge of the thermo-optic coefficients κ_R and κ_A provides a better understanding of the origin of the thermotransmittance signal. With our new approach, future works will focus on the measurement of quantitative 3D temperature fields in semi-transparent materials. In addition, the ability to differentiate between

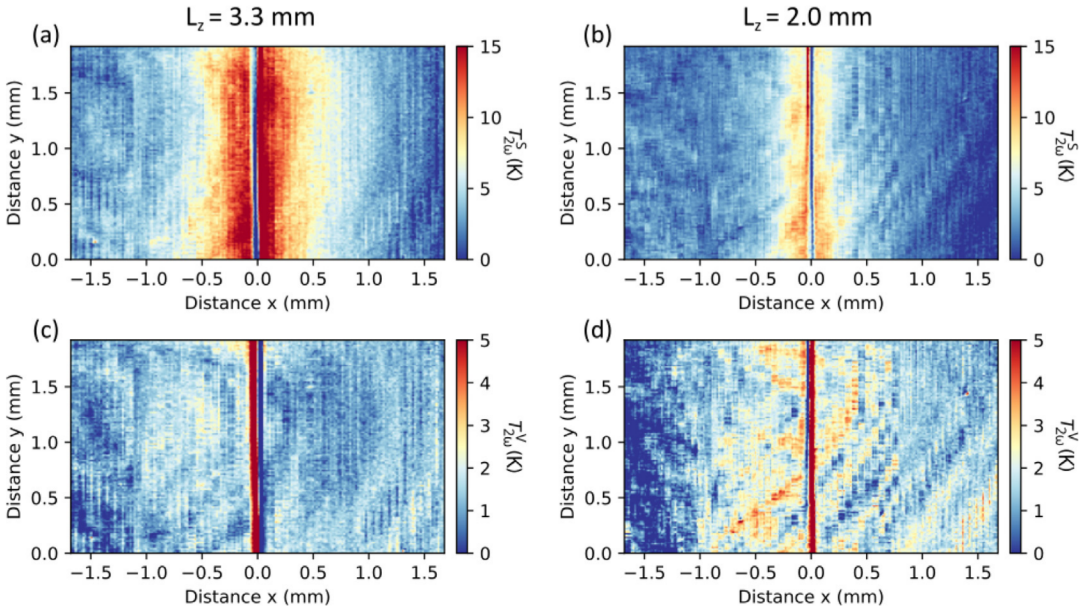

Fig. 7. Measured temperature variation maps of the surface and average volume of the Borofloat samples: (a) and (c) surface and average volume temperature maps of the sample with a thickness of 3.3 mm and (b) and (d) surface and average volume temperature maps of the sample with a thickness of 2 mm.

absorbance and reflectance contributions within the thermotransmittance signal would enable us to derive the thermal resistances across multiple semitransparent layers.

CRediT authorship contribution statement

C. Bourgès: Writing – review & editing, Writing – original draft, Visualization, Validation, Project administration, Methodology, Investigation, Formal analysis, Data curation, Conceptualization,. **J. Maire:** Writing – review & editing, Writing – original draft, Visualization, Validation, Supervision, Project administration, Methodology, Investigation, Funding acquisition, Formal analysis, Conceptualization,. **S. Chevalier:** Writing – review & editing, Writing – original draft, Visualization, Validation, Supervision, Project administration, Methodology, Investigation, Funding acquisition, Formal analysis, Conceptualization. **S. Dilhaire:** Writing – review & editing, Writing – original draft, Visualization, Validation, Supervision, Project administration, Methodology, Investigation, Funding acquisition, Formal analysis, Conceptualization,.

Declaration of competing interest

The authors declare the following financial interests/personal relationships which may be considered as potential competing interests: J. Maire reports financial support was provided by French National Research Agency. If there are other authors, they declare that they have no known competing financial interests or personal relationships that could have appeared to influence the work reported in this paper.

Data availability

Data will be made available on request.

Acknowledgments

This work was supported by the French National Research Agency (ANR) (Grant No. ANR-22-CE50-0015) and the Nouvelle Aquitaine local government, France (Grant No. AAPR2021-2020-12035510).

Appendix A. Thermotransmittance expression

First, the temperature variations of the reflectance, R, and absorbance, α, are given by Eqs. (A.1) and (A.2). R_0 and α_0 are the reflectance and absorbance at ambient temperature, respectively; T_0 and κ_i are proportionality coefficients; and $\Delta T = T - T_0$.

$$R(T) = R_0(1 + \kappa_1 \Delta T) \tag{A.1}$$

$$\alpha(T) = \alpha_0(1 + \kappa_2 \Delta T) \tag{A.2}$$

Consequently, in the general case with a temperature gradient along the thickness of the material, the transmittance Γ as a function of temperature is given by Eq. (A.3). Here, T_1^S is the temperature of the top surface, and T_2^S is the temperature of the back surface of the sample.

$$\Gamma(T) = (1 - R(T_1^S))(1 - R(T_2^S))e^{-\int_0^{L_z} \alpha(T(z))dz} \tag{A.3}$$

The thermotransmittance ratio, $\Delta\Gamma/\Gamma_0$, can be expressed as:

$$\frac{\Delta\Gamma(T)}{\Gamma_0} = \frac{(1 - R(T_1^S))(1 - R(T_2^S))e^{-\alpha_0\kappa_2 \int_0^{L_z} \Delta T(z)dz}}{(1 - R_0)^2} - 1 \tag{A.4}$$

Linearizing the exponential function and considering the first-order approximation with respect to ΔT results in the following equation:

$$\frac{\Delta\Gamma(T)}{\Gamma_0} \approx \underbrace{-\frac{R_0\kappa_1}{1 - R_0}}_{\kappa_R}(\Delta T_1^S + \Delta T_2^S)\underbrace{-\alpha_0\kappa_2}_{\kappa_A}\int_0^{L_z} \Delta T(z)dz \tag{A.5}$$

Appendix B. Negligible impact of convective losses on temperature variations

In our previous work [24], it was demonstrated that convective losses have a negligible impact on temperature variations at different frequencies 2ω. Fig. B.8 compares the amplitude and phase of temperature variations with and without considering convective losses.

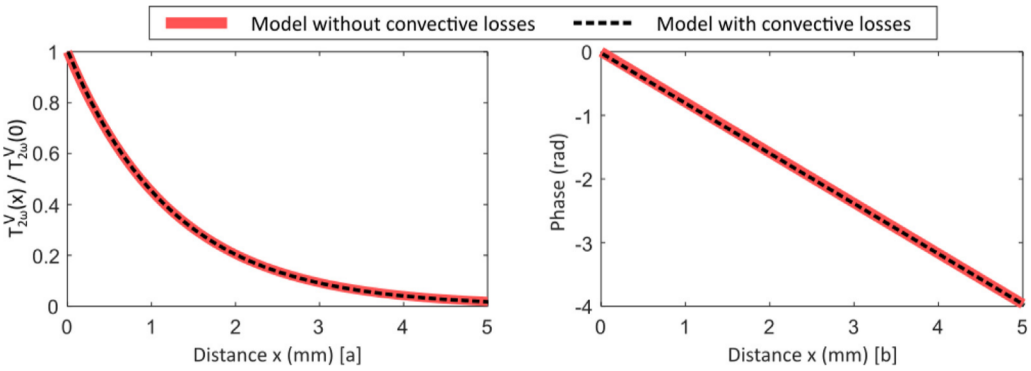

Fig. B.8. Normalized amplitude (a) and phase (b) of the temperature profile within a 2.0 mm thick sample, with or without convective losses. The calculations were conducted using a convective coefficient of $h = 20$ W/m^2/K.

References

[1] S. Ma, M. Jiang, T. Peng, C. Song, J. Wu, J. Wang, T. Deng, W. Shang, Temperature Effect and thermal Impact in lithium-ion Batteries: a review, Progr. Nat. Sci.: Mater. Int. 28 (6) (2018) 653–666, http://dx.doi.org/10.1016/j.pnsc.2018.11.002.

[2] X. Maldague, S. Marinetti, Pulse phase infrared thermography, J. Appl. Phys. 79 (5) (1996) 2694–2698, http://dx.doi.org/10.1063/1.362662.

[3] J.-L. Battaglia, A. Kusiak, V. Schick, A. Cappella, C. Wiemer, M. Longo, E. Varesi, Thermal characterization of the SiO2-Ge2Sb2Te5 interface from room temperature up to 400 °C, J. Appl. Phys. 107 (4) (2010) 044314, http://dx.doi.org/10.1063/1.3284084.

[4] A. Scalbi, F. Bozzoli, L. Cattani, G. Inglese, M. Malavasi, R. Olmi, Thermal imaging of inaccessible interfaces, Infrared Phys. Technol. 125 (2022) 104268, http://dx.doi.org/10.1016/j.infrared.2022.104268.

[5] R. Usamentiaga, P. Venegas, J. Guerediaga, L. Vega, J. Molleda, F.G. Bulnes, Infrared thermography for temperature measurement and Non-Destructive testing, Sensors 14 (7) (2014) 12305–12348, http://dx.doi.org/10.3390/s140712305.

[6] D.G. Cahill, K.E. Goodson, A. Majumdar, Thermometry and thermal transport in Micro/Nanoscale Solid-State devices and structures, J. Heat Transfer 124 (2) (2001) 223–241, http://dx.doi.org/10.1115/1.1454111.

[7] D.U. Kim, K.S. Park, C.B. Jeong, G.H. Kim, K.S. Chang, Quantitative temperature measurement of multi-layered semiconductor devices using spectroscopic thermoreflectance microscopy, Opt. Express 24 (13) (2016) 13906, http://dx.doi.org/10.1364/oe.24.013906.

[8] D. Anthony, D. Sarkar, A. Jain, Contactless, non-intrusive core temperature measurement of a solid body in steady-state, Int. J. Heat Mass Transfer 101 (2016) 779–788, http://dx.doi.org/10.1016/j.ijheatmasstransfer.2016.05.073.

[9] M.-M. Groz, A. Sommier, E. Abisset, S. Chevalier, J.-L. Battaglia, J.-C. Batsale, C. Pradère, Thermal resistance field estimations from IR thermography using multiscale Bayesian inference, Quant. InfraRed Thermogr. 18 (5) (2020) 332–343, http://dx.doi.org/10.1080/17686733.2020.1771529.

[10] M.-M. Groz, E. Abisset-Chavanne, A. Méziane, A. Sommier, C. Pradère, Three-dimensional reconstruction of thermal volumetric sources from surface temperature fields measured by infrared thermography, Appl. Sci. 9 (24) (2019) 5464, http://dx.doi.org/10.3390/app9245464.

[11] J. Gieseler, A. Adibekyan, C. Monte, J. Hollandt, Apparent emissivity Measurement of semi-transparent materials Part 2: Theoretical concept, J. Quant. Spectrosc. Radiat. Transfer 258 (2021) 107317, http://dx.doi.org/10.1016/j.jqsrt.2020.107317.

[12] O. Rozenbaum, D. De Sousa Meneses, Y. Auger, S. Chermanne, P. Echegut, A spectroscopic method to measure the spectral emissivity of semi-transparent materials up to high temperature, Rev. Sci. Instrum. 70 (10) (1999) 4020–4025, http://dx.doi.org/10.1063/1.1150028.

[13] V. Rieke, K.B. Pauly, MR thermometry, J. Magn. Reson. Imaging 27 (2) (2008) 376–390, http://dx.doi.org/10.1002/jmri.21265.

[14] C. Mougenot, B. Quesson, B.D. De Senneville, P.L. De Oliveira, S.M. Sprinkhuizen, J. Palussière, N. Grenier, C. Moonen, Three-dimensional spatial and temporal temperature control with MR Thermometry-guided Focused Ultrasound (MRGHIFU), Magn. Reson. Med. 61 (3) (2008) 603–614, http://dx.doi.org/10.1002/mrm.21887.

[15] S. Norton, L. Testardi, H. Wadley, Reconstructing internal temperature distributions from ultrasonic time-of-flight tomography and dimensional resonance measurements, in: 1983 Ultrasonics Symposium, 1983, pp. 850–855, http://dx.doi.org/10.1109/ULTSYM.1983.198180.

[16] R. Richardson, P. Ireland, D.A. Howey, Battery internal temperature estimation by combined impedance and surface temperature measurement, J. Power Sources 265 (2014) 254–261, http://dx.doi.org/10.1016/j.jpowsour.2014.04.129.

[17] J.B. Robinson, J.A. Darr, D.S. Eastwood, G. Hinds, P. Lee, P.R. Shearing, O.O. Taiwo, D.J.L. Brett, Non-uniform temperature distribution in li-ion batteries during discharge – a combined thermal imaging, x-ray micro-tomography and electrochemical impedance approach, J. Power Sources 252 (2014) 51–57, http://dx.doi.org/10.1016/j.jpowsour.2013.11.059.

[18] Y.S. Hsiao, C.X. Deng, Calibration and evaluation of ultrasound thermography using infrared imaging, Ultrasound Med. Biol. 42 (2) (2016) 503–517, http://dx.doi.org/10.1016/j.ultrasmedbio.2015.09.021.

[19] C. Bourges, S. Chevalier, J. Maire, A. Sommier, C. Pradère, S. Dilhaire, Infrared thermotransmittance-based temperature field measurements in semitransparent media, Rev. Sci. Instrum. 94 (3) (2023) http://dx.doi.org/10.1063/5.0131422.

[20] C. Bourges, S. Chevalier, J. Maire, A. Sommier, C. Pradere, S. Dilhaire, Mid-infrared spectroscopic thermotransmittance measurements in dielectric materials for thermal imaging, Appl. Phys. Lett. 124 (1) (2024) 012202, http://dx.doi.org/10.1063/5.0176689.

[21] R. Rosei, M. Meuti, C. Coluzza, C. Quaresima, Thermotransmission measurements on self-supporting metal films, Opt. Lett. 1 (6) (1977) 217, http://dx.doi.org/10.1364/ol.1.000217.

[22] N. Kakuta, Y. Arakawa, M. Kyoda, T. Miyake, K. Mishiba, K. Kondo, Near-infrared measurement of axisymmetric temperature field formed by free convection from a 1-mm-diameter heating sphere in water, Int. J. Heat Mass Transfer 137 (2019) 847–856, http://dx.doi.org/10.1016/j.ijheatmasstransfer.2019.03.127.

[23] M.S. Bensalem, A. Sommier, J.-C. Mindeguia, J.-C. Batsale, L.-D. Patino-Lope, C. Pradère, Contactless transient THZ temperature imaging by thermo-transmittance technique on semi-transparent materials, J. Infrared Millimeter Terahertz Waves 39 (11) (2018) 1112–1126, http://dx.doi.org/10.1007/s10762-018-0521-3.

[24] C. Bourges, Thermography in Semitransparent Media Based on Mid-Infrared Thermotransmittance (Theses), Université de Bordeaux, 2023, 2023BORD0206, URL https://theses.hal.science/tel-04228284.

[25] O.M. Corbino, Periodic variation of resistance of metallic filaments on alternating current, Atti della Reale Accademia Nazionale dei Lincei 20 (1911) 222–228.

[26] D.G. Cahill, Thermal conductivity measurement from 30 to 750 K: the 3omega method, Rev. Sci. Instrum. 61 (2) (1990) 802–808, http://dx.doi.org/10.1063/1.1141498.

[27] D. Maillet, S. André, J.C. Batsale, A. Degiovanni, C. Moyne, Thermal Quadrupoles: Solving the Heat Equation through Integral Transforms, Wiley, 2000.

[28] S.T.G.S. GmbH, Schott Borofloat 33, 2009.

[29] T. Kariya, H. Kurata, Generalized Least Squares, Wiley, 2004.